remote sensing

MDPI

Article

Mapping Seagrass Distribution and Abundance: Comparing Areal Cover and Biomass Estimates Between Space-Based and Airborne Imagery

Victoria J. Hill [1,*], Richard C. Zimmerman [1], Dorothy A. Byron [2] and Kenneth L. Heck, Jr. [2]

[1] Department of Ocean & Earth Sciences, Old Dominion University, Norfolk, VA 23529, USA; rzimmerm@odu.edu
[2] Dauphin Island Sea Lab, 101 Bienville Blvd, Dauphin Island, AL 36528, USA; dbyron@disl.edu (D.A.B.); kheck@disl.org (K.L.H.J.)
* Correspondence: vhill@odu.edu

Abstract: This study evaluated the effectiveness of Planet satellite imagery in mapping seagrass coverage in Santa Rosa Sound, Florida. We compared very-high-resolution aerial imagery (0.3 m) collected in September 2022 with high-resolution Planet imagery (~3 m) captured during the same period. Using supervised classification techniques, we accurately identified expansive, continuous seagrass meadows in the satellite images, successfully classifying 95.5% of the 11.18 km^2 of seagrass area delineated manually from the aerial imagery. Our analysis utilized an occurrence frequency (*OF*) product, which was generated by processing ten clear-sky images collected between 8 and 25 September 2022 to determine the frequency with which each pixel was classified as seagrass. Seagrass patches encompassing at least nine pixels (~200 m^2) were almost always detected by our classification algorithm. Using an *OF* threshold equal to or greater than >60% provided a high level of confidence in seagrass presence while effectively reducing the impact of small misclassifications, often of individual pixels, that appeared sporadically in individual images. The image-to-image uncertainty in seagrass retrieval from the satellite images was 0.1 km^2 or 2.3%, reflecting the robustness of our classification method and allowing confidence in the accuracy of the seagrass area estimate. The satellite-retrieved leaf area index (LAI) was consistent with previous in situ measurements, leading to the estimate that 2700 tons of carbon per year are produced by the Santa Rosa Sound seagrass ecosystem, equivalent to a drawdown of approximately 10,070 tons of CO_2. This satellite-based approach offers a cost-effective, semi-automated, and scalable method of assessing the distribution and abundance of submerged aquatic vegetation that provides numerous ecosystem services.

Keywords: seagrass mapping; remote sensing; satellite imagery; aerial imagery

Citation: Hill, V.J.; Zimmerman, R.C.; Byron, D.A.; Heck, K.L., Jr. Mapping Seagrass Distribution and Abundance: Comparing Areal Cover and Biomass Estimates Between Space-Based and Airborne Imagery. *Remote Sens.* **2024**, *16*, 4351. https://doi.org/10.3390/rs16234351

Academic Editors: Jiayi Pan and Zhe-Wen Zheng

Received: 25 September 2024
Revised: 10 November 2024
Accepted: 13 November 2024
Published: 21 November 2024

1. Introduction

Submerged aquatic vegetation (SAV), including both freshwater and marine species, plays a crucial role in maintaining the health and balance of coastal environments worldwide [1]. From providing habitats and nursery grounds for a diverse array of species [2,3] to attenuating wave energy [4–7], stabilizing sediments [8,9], and mitigating coastal erosion [10], seagrasses contribute significantly to the resilience and productivity of coastal ecosystems [11]. They also represent important blue carbon resources worldwide [12]. Despite their ecological significance, seagrass meadows face numerous threats, including coastal development, pollution, and climate-change-induced stressors. Accurate mapping of seagrass distribution and density is critical in assessing the health and extent of these ecosystems and facilitating decision-making in conservation and management efforts [13,14].

SAV populations are mapped infrequently in most locations due to the high cost and logistical challenges associated with traditional aerial and in situ campaigns. Infrequent

mapping with relatively long temporal gaps spanning multiple years limits our ability to identify the causes of observed change. The Chesapeake Bay (Virginia, USA) and Tampa Bay (Florida, USA) SAV mapping programs have maintained long-term annual or biannual mapping efforts going back as far as the 1970s that provide important temporal information on SAV status and trends [13,15,16]. However, even these programs are logistically restricted to capturing SAV distribution only once a year, often in the summer season. Consequently, the inability to track variations at frequencies higher than once per year, particularly in dynamic coastal environments where the SAV coverage can fluctuate seasonally or with extreme events [17], represents a significant gap in our understanding and can hinder management initiatives. In addition, the radiometrically uncalibrated imagery provided by most aerial campaigns requires the manual identification of SAV using hand-drawn polygons and the semi-quantitative delineation of different density classes based on percent cover [13,15]. Because the polygons with densities <100% necessarily include pixels of bare sand, the total area recovered from these manual analyses can overestimate the actual SAV distribution by 50% or more, particularly in the low-density polygons [18]. Finally, it is impossible to generate statistically reliable uncertainty estimates for any given year from single images collected with such long (annual to decadal) repeat times.

Satellites can provide the higher-frequency mapping (daily, weekly, or monthly) needed to monitor seasonal and annual trends in SAV and provide statistically valid estimates of uncertainties in areal extent and plant density retrieved from the imagery. Several high-resolution ($\leq$30 m) satellites have been used to map seagrasses successfully, including Landsat [19,20], IKONOS [21], Quickbird-2 [22,23], RapidEye, WorldView-2 and -3 [24–26], Sentinel-2 [27], and Planet [28]. Satellite and aerial imagery each have unique strengths and limitations in SAV monitoring, largely due to differences in spatial and temporal resolution. Satellites, like those in the Planet constellation, capture imagery at high frequencies—often daily or near-daily—which is essential in observing short-term changes in SAV due to changes in water quality, storms, or seasonal growth patterns. However, the spatial resolution of satellite imagery (e.g., 3–30 m) can make it challenging to accurately resolve smaller or patchier seagrass beds. This limitation can lead to the underestimation of SAV in areas with sparse or fragmented coverage, as smaller patches may fall below the resolution threshold and appear as false negatives. In contrast, aerial imagery offers a much finer spatial resolution, often down to 0.5 m or better, which allows for the detailed mapping of small or sparse SAV patches. However, the low temporal frequency limits the ability to track rapid changes over time. Integrating satellite imagery, with its synoptic coverage and high temporal frequency, alongside the less frequent but extremely fine resolution of aerial and drone imagery, holds great potential for enhancing the accuracy and scope of seagrass monitoring and blue carbon assessments [29]. However, to use satellite imagery effectively for regular seagrass monitoring, it is essential to understand how its measurements differ from the long-term aerial record to ensure consistency and accuracy in tracking changes over time.

In this study, we compare high-resolution (0.3 m) aerial imagery collected over Santa Rosa Sound in Florida in September of 2022 with Planet imagery (3 m resolution) collected during the same month to assess differences in the total area recovered and SAV detection limitations between the two imaging systems. Additionally, we provide estimates of seagrass above-ground and below-ground biomass from the radiometrically calibrated and atmospherically corrected Planet imagery, values which cannot be retrieved from uncalibrated aerial imagery classified into hand-drawn polygons.

2. Methods

2.1. Study Area

Santa Rosa Sound is a semi-enclosed coastal lagoon separated from the Gulf of Mexico by a barrier island running west to east for about 47 km at the southern end of Pensacola Bay, Florida (Figure 1). Seagrass extends along the northern shore of the Sound, from the western edge all the way to the bridge at Navarre. The southern shore of the Sound

on the lee side of the barrier island supports many large continuous seagrass meadows separated by stretches of shallow submerged sand that are home to sparsely scattered small patches of seagrass. *Thalassia testudinum* (turtlegrass) is the dominant and most widely distributed species. *Halodule wrightii* (shoal grass) is found in small patches, particularly in the shallowest water and in disturbed areas [30–32]. Aerial surveys conducted at 10-to-20-year intervals since 1960 indicate that the total seagrass area declined dramatically from 1960 to 1980 but has been somewhat stable since then [32,33].

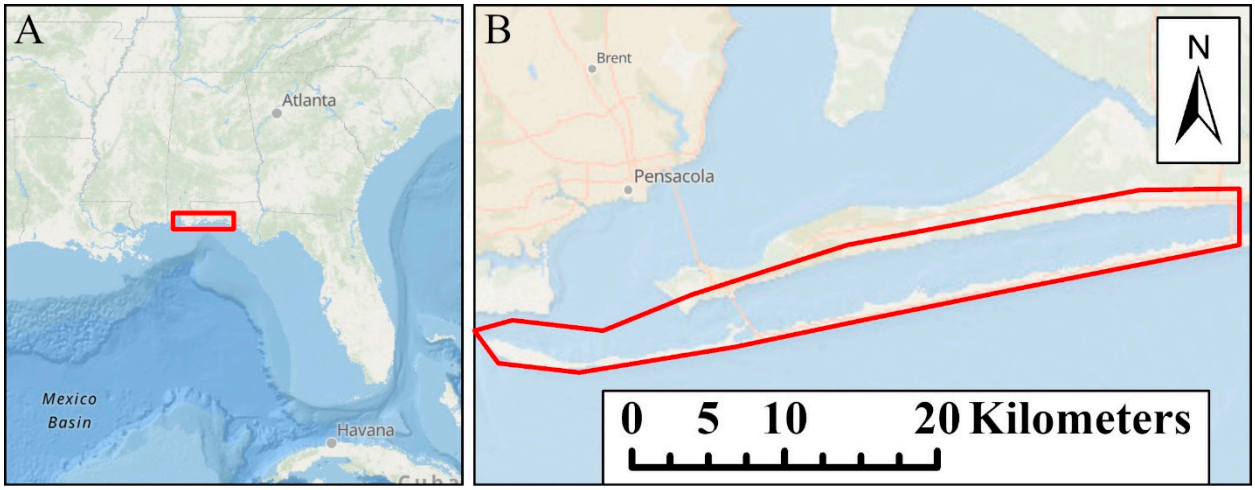

Figure 1. (**A**). The location of Pensacola Bay is indicated by the red box. (**B**). The location of Santa Rosa Sound is indicated by the red outline. Underlying Ocean basemap from Esri.ArcGIS Pro 3.3.2. Sources: Esri.Arc, GEBCO, NOAA, National Geographic, DeLorme, HERE, Geonames.org, and other contributors.

2.2. Aerial Photography (Copied from NV5 Report)

Aerial photographic surveys and image processing equivalent to NASA Level 2B were performed by the geospatial services company *NV5* over Pensacola Bay in September 2022 (Figure 1A). Santa Rosa Sound (Figure 1B) was surveyed on 22 September 2022. The aircraft flew a Microsoft UltraCam Eagle M34, with 4 channels (RGB and NIR), at 3800 m, which provided imagery with a 15 cm ground sampling distance. Relative radiometric calibration and geometric correction were applied to the raw images using the camera's calibration files. The resulting radiometry was manually edited to ensure that each image had the appropriate tone and to blend each image with neighboring images. Once the radiometry was edited, the separate RGBI and Panchromatic images were blended together to form single-level 4-band TIFF images. This dataset was produced to meet ASPRS Positional Accuracy Standards for Digital Geospatial Data [34] for a 1.2 (m) RMSEx/RMSEy Horizontal Accuracy Class A. The image radiometric values were calibrated to specific gain and exposure settings associated with each capture using Microsoft's UltraMap software suite. The calibrated images were saved in TIFF format for input to subsequent processes. The photograph position and orientation were calculated by linking the time of image capture, the corresponding aircraft position and attitude, and the smoothed best estimate of trajectory (SBET) data in Applanix POSPac mapping software. Aerotriangulation was then performed using ImageStation AT (IS AT). Adjusted images were then draped upon a ground model and orthorectified. Individual orthorectified tiffs were blended together to remove seams and corrected for any remaining radiometric differences between images using Inpho's OrthoVista; the final image resolution was 0.3 m.

2.3. Planet Satellite Imagery

All satellite images were downloaded from the Planet data archive as radiometrically calibrated, atmospherically corrected, geolocated, and Sentinel-harmonized 8-band imagery

(equivalent to NASA Level 2B). Ten cloud-free, low-turbidity images of various parts of Santa Rosa Sound were obtained on nine days between 8 and 25 September 2022 that coincided with the aerial photographic surveys (Figure 2, Table 1). No single satellite image captured the entire study area, because the 47 km extent of Santa Rosa Sound is wider than the swath width (25 to 32.5 km) of the Dove satellites. The sole satellite pass on the day that the aerial images were taken (22 September 2022) was excluded from the analysis because it covered only a small portion at the mouth of the Sound. All image processing was conducted on an 11th Gen Intel® Core™ i7-1185G7 laptop using ArcGIS Pro 3.3.2 software.

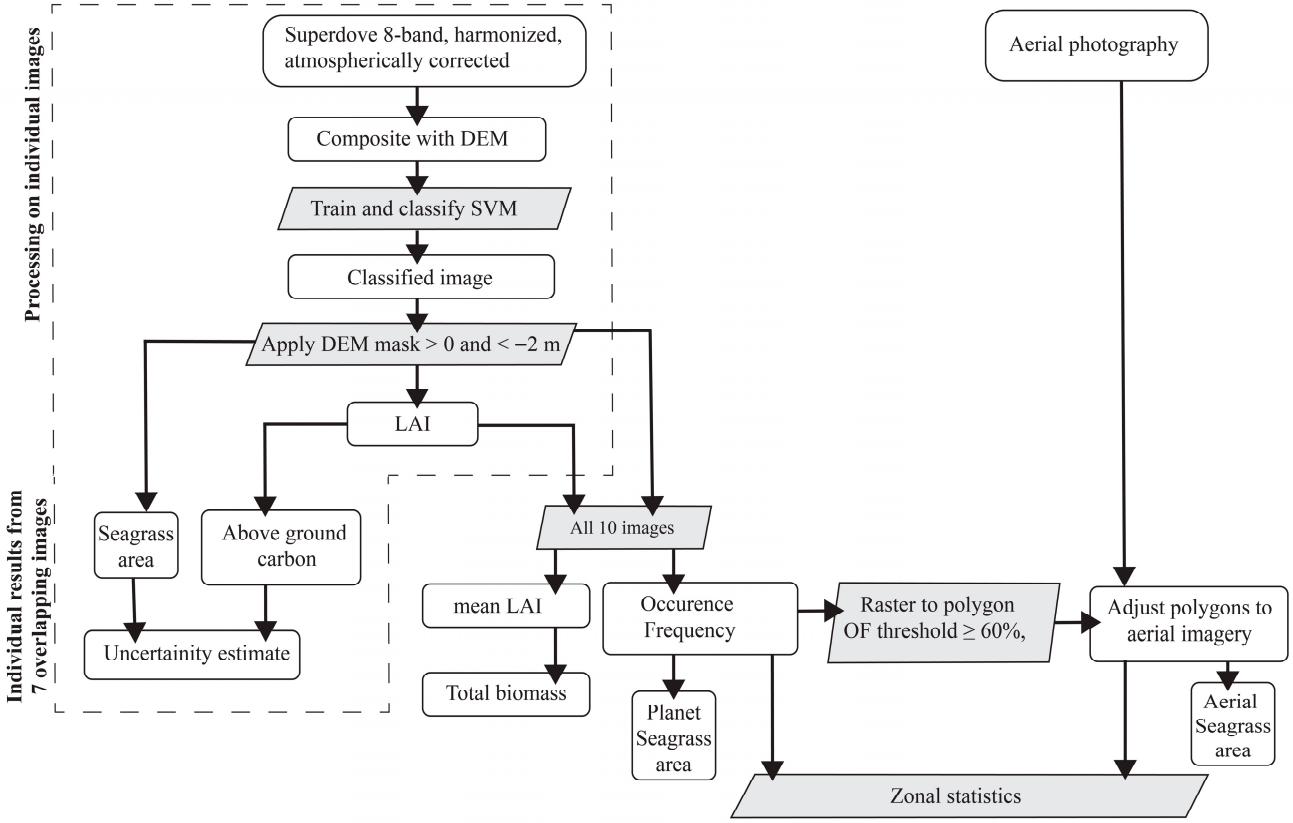

Figure 2. Flowchart outlining the processing steps for satellite and aerial imagery.

Table 1. Planet image acquisition information and tidal state for Santa Rosa Sound. Images collected on 9/13 were from two different sensors and were processed separately.

Image Acquisition Date and Time (GMT)	Tidal State Relative to MLLW (m)
8 September 202216:07	0.547
13 September 2022 15:30	0.229
13 September 2022 16:18	0.227
15 September 2022 16:04	0.21
16 September 2022 16:03	0.236
17 September 2022 16:04	0.277
18 September 2022 16:05	0.328
19 September 2022 15:31	0.402
20 September 2022 16:05	0.424
25 September 2022 15:31	0.37

2.3.1. Image Preprocessing

The 8-band images were combined with a digital elevation model (DEM) downloaded from NOAA's Continuously Updated Digital Elevation Model [35] at NAV88 vertical datum and 3 m spatial resolution. The bathymetry raster data were converted to the mean low

lower water (MLLW) tidal datum using the NOAA vertical datum transformation tool (https://vdatum.noaa.gov, accessed on 1 August 2024) and reprojected to WGS 1984 UTM Zone 16N. The bathymetry raster was then composited with the 8-band satellite imagery using the ArcGIS Pro composite bands tool to generate the 9-band raster files used in the classification process (Figure 2).

2.3.2. Classification

The supervised classification of each Planet image was performed using the support vector machine (SVM) algorithm in ArcGIS Pro (Figure 2). An overall schema for the study region was developed for seven classes: (i) seagrass (57 patches), (ii) submerged bare sand (32 patches), (iii) optically deep water (24 patches), (iv) dry beach sand above the water (8 patches), (v) terrestrial vegetation (7 patches), and (vii) urban landcover (4 patches). Rectangular polygons of each class referred to as regions of interest (ROIs) were identified manually throughout Santa Rosa Sound using a combination of local knowledge and visual interpretation. ROIs were chosen to cover variability in spectral characteristics within the same target throughout the region, i.e., sparse seagrass and dense seagrass were both captured within the seagrass target ROIs. Targets with greater spectral variation, such as seagrass, submerged bare sand, and deep water, required more training patches for classification.

The SVM algorithm was trained on each individual image using the target patches prior to classification. After classification, the DEM was used to remove all pixels shallower than 0 m (intertidal and dry-land) and deeper than the 2 m depth threshold for seagrass growth in this region (Figure 2); this reduced the misclassifications that occurred in small terrestrial ponds and in deeper water.

An occurrence frequency (*OF*) map was generated by calculating the percentage with which each pixel was identified as seagrass throughout all 10 available images (Figure 2), as follows:

$$OF = \frac{Number\ of\ times\ a\ pixel\ was\ classified\ as\ SAV}{Number\ of\ times\ the\ pixel\ was\ imaged} \times 100 \quad (1)$$

Utilizing the frequency with which a pixel was classified as seagrass effectively mitigated individual misclassifications occurring sporadically within each scene, ensuring a robust confidence in seagrass presence, contingent upon the selected *OF* threshold. The total area of seagrass was then calculated for *OF* thresholds ≥60%, ≥70%, ≥80%, and ≥90%.

2.3.3. Building a Ground Truth Map

The seagrass presence map generated from an *OF* threshold of ≥60% was used to aggregate the classified pixels into polygons representing the extent of each individual seagrass meadow using the raster-to-polygon tool in ArcGIS Pro 3.3.2. The polygons were overlaid on the aerial imagery and adjusted where necessary to depict the full extent of each seagrass meadow as seen in the aerial imagery. Any discrepancies, such as patches observed in the aerial imagery but not captured in the Planet-derived polygons, were hand-delineated and incorporated into the layer. Comparative analysis between the distribution of seagrass at various *OF* thresholds and the aerial polygon layer was conducted utilizing the Zonal Statistics as a Table tool in ArcGIS Pro, which calculates the area of seagrass-classified pixels within each aerial polygon.

2.3.4. Leaf Area Index and Carbon Retrieval

The leaf area index (LAI, m^2 leaf m^{-2} ground) was retrieved for each image using methodology from [36,37], where seagrass canopy reflectance (R_c) was derived from the remote sensing reflectance (R_{rs}) of Planet Band 4 (547–583 nm) and the water column optical properties and water depth at the time of the satellite pass (Equation (1)). The water depth (z_b) at the time of image acquisition was calculated using the DEM described

above, corrected using tide predictions for Fishing Bend in Santa Rosa Sound (NOAA Stn ID 8729806, Table 1).

$$R_b(band4) = \frac{R_{rs}(band4)Q_b}{\tau_u} \frac{exp\left[\overline{-K_{lu}(z_b)}\, z_b\right]}{exp(-K_d\ z_b)} \quad (2)$$

Downwelling diffuse attenuation (K_d) and depth-averaged upwelling radiance attenuation $\left[\overline{-K_{lu}(z_b)}\right]$ coefficients were modeled using *Hydrolight* (© C. Mobley, Sequoia Scientific) parameterized with the average Chlorophyll *a* (1.26 mg·m^{-3}) and total suspended sediment (5 mg·m^{-3}) observations from Santa Rosa Sound collected in June, July, and September of 2016 [38]. Q_b represents the ratio of upwelling irradiance (E_u) to upwelling radiance (L_u) at the base of the water column and was set to π on the assumption that the bottom reflectance was Lambertian [39]. The relative transmittance of L_u across the water–air interface (τ_u) was approximated as 0.54 [40].

The leaf area index (LAI) was calculated from R_c using a relationship developed in turtlegrass systems along the Gulf of Mexico Florida coastline [37]. Above-ground seagrass biomass (Equation (3)) was estimated from LAI using published data from studies in Santa Rosa Sound [38], the dry weight (Equation (4)) and dry-weight-to-carbon ratio (Equation (5)) were estimated based on data collected in tropical turtlegrass beds [41–43] and the conversion between the above- and below-ground dry weight (Equation (6)) was estimated based on data collected in Santa Rosa Sound [44]. The below-ground carbon stock was calculated using the same dry-weight-to-carbon ratio as the above-ground biomass. The LAI, biomass, and carbon reported in the results are the mean values calculated from all ten processed images.

$$Above\ ground\ Fresh\ Wt\ (\text{g FW}) = 330\ \left(\text{g m}^{-2}\text{leaf}\right) \times LAI \quad (3)$$

$$Above\ ground\ Dry\ Wt\ (\text{g DW}) = fresh\ Wt \times 0.2\ \left(\text{g DW g}^{-1}\text{g FW}^{-1}\right) \quad (4)$$

$$Above\ ground\ seagrass\ carbon\ stock\ (\text{g C}) = dry\ wt\ (\text{g DW}) \times 0.35\ \left(\text{g C g DW}^{-1}\right) \quad (5)$$

$$Below\ ground\ dry\ weight\ (\text{g DW}) = Above\ ground\ Dry\ Wt \times 2 \quad (6)$$

2.3.5. Statistical Confidence of the Retrieval Estimates

The presence of multiple satellite images of the same area collected within a few days of each other provided an opportunity to estimate the statistical uncertainty in our satellite retrievals of seagrass cover and density that could not be achieved from single-pass aerial imagery. Seven of the ten Planet images used here had sufficient overlap to estimate the uncertainty in determining the areal extent and density of seagrass. Images from 8, 13, 17, 18, 19, 20, and 25 September were clipped to a 30.7 Km^2 subset common to all images (Figure 3, white-dashed box). The mean and 95% confidence intervals for total seagrass cover and above-ground carbon stored in seagrass (total $AGC_{seagrass}$) were then calculated from all seven images.

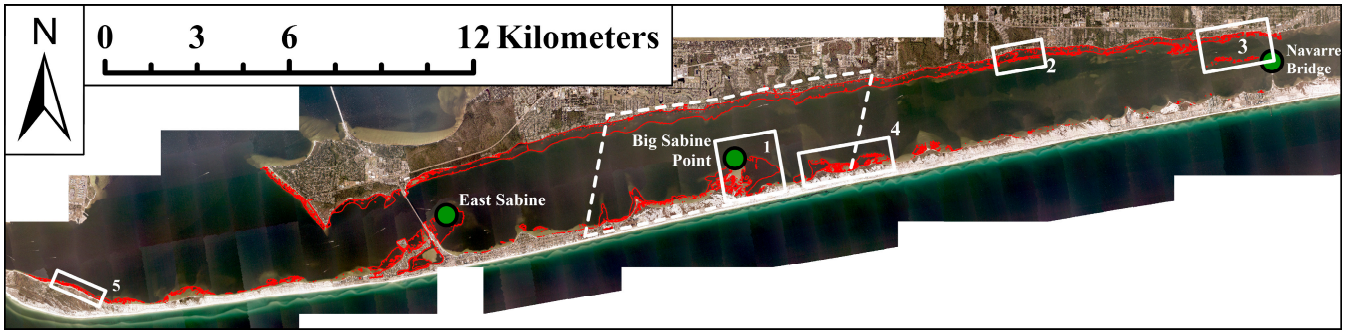

Figure 3. Aerial imagery with areas identified as containing seagrass overlaid as polygons (red). The white-dashed box is the location of image overlap used in uncertainty estimates; solid white boxes numbered 1 through 5 are the locations of examples shown later figures. Green dots highlight the locations of East Sabine and Big Sabine Point, mentioned later in the text.

3. Results

3.1. Comparison of Aerial and Planet Seagrass Distribution

Seagrass was present throughout Santa Rosa Sound in large continuous meadows and a few areas of sparse small patches (Figure 3). A total of 11.18 km^2 of seagrass cover was identified from the aerial imagery. Most of the seagrass was present within expansive, uninterrupted meadows. There were thirteen large, continuous meadows >0.1 km^2 in area that accounted for 87% of the total seagrass cover (Table 2). The largest continuous seagrass meadow present along the northern shore encompassed 6.6 km^2. Although our analysis identified 625 meadows/patches smaller than 0.01 km^2 (~1000 pixels), collectively, they represented <5% of the total area.

Table 2. Size distribution of seagrass polygons from the aerial imagery and percent contribution to the total seagrass area.

Polygon Area (km^2)	Number of Polygons	Percent Contribution to Total Area
<0.001	491	2.53
0.001–0.01	134	3.14
0.01–0.1	29	7.28
0.1–1	13	28.71
>1	1	58.34

The seagrass area identified from Planet images ranged from 11.29 km^2 at an *OF* threshold of ≥60% to 9.59 Km^2 at an *OF* threshold of ≥90% (Table 3). An *OF* threshold of ≥60% captured 95.5% of seagrass identified in the aerial imagery (Table 3), with 0.62 km^2 of false-positive seagrass identifications and 0.5 Km^2 of false-negative seagrass identifications. Increasing the stringency of the *OF* threshold reduced the percentage of seagrass that was correctly classified (85.6% for $OF \geq 90\%$), as well as reducing false positives. Differences in seagrass area with different *OF* thresholds stemmed primarily from false-positive classifications at lower *OF* along the deep edges of seagrass beds close to Navarre Bridge (Figure 4A) and false-negative classifications at higher *OF* in spare meadows close to the mouth of Santa Rosa Sound (Figure 4B).

At an $OF \geq 60\%$, only 0.11 km^2 (0.95%) of false-negative area was present in completely unresolved seagrass patches (Table 3). The remaining area was represented by false-negative pixels in otherwise partly resolved seagrass patches, mainly in sparse seagrass coverage where part of the patch was resolved (Figure 4B). The area of unresolved patches increased to 0.17 km^2 (1.61% of the aerial polygons) at an *OF* threshold of 90% (Table 3). The polygons containing no pixels classified as seagrass in the Planet imagery were all smaller than 1000 m^2 (111 pixels), with the majority smaller than 100 m^2 (11 pixels) (Figure 5).

Table 3. Seagrass area retrieved from Planet imagery for different occurrence frequencies compared to the seagrass area of 11.18 Km^2 derived from aerial imagery. Values in square brackets in the false-negative column represent the false-negative area of seagrass patches in which no pixels were identified as seagrass.

Planet Occurrence Frequency (%)	Total Planet Area (km^2)	True-positive Area (km^2)	False-positive Area (km^2)	False-Negative Area (km^2)	% of Aerial Captured by Planet
≥60	11.29	10.68	0.62	0.50 [0.11]	95.5
≥70	10.64	10.49	0.15	0.69 [0.12]	93.8
≥80	10.28	10.26	0.02	0.92 [0.14]	91.8
≥90	9.59	9.59	0.007	1.59 [0.17]	85.7

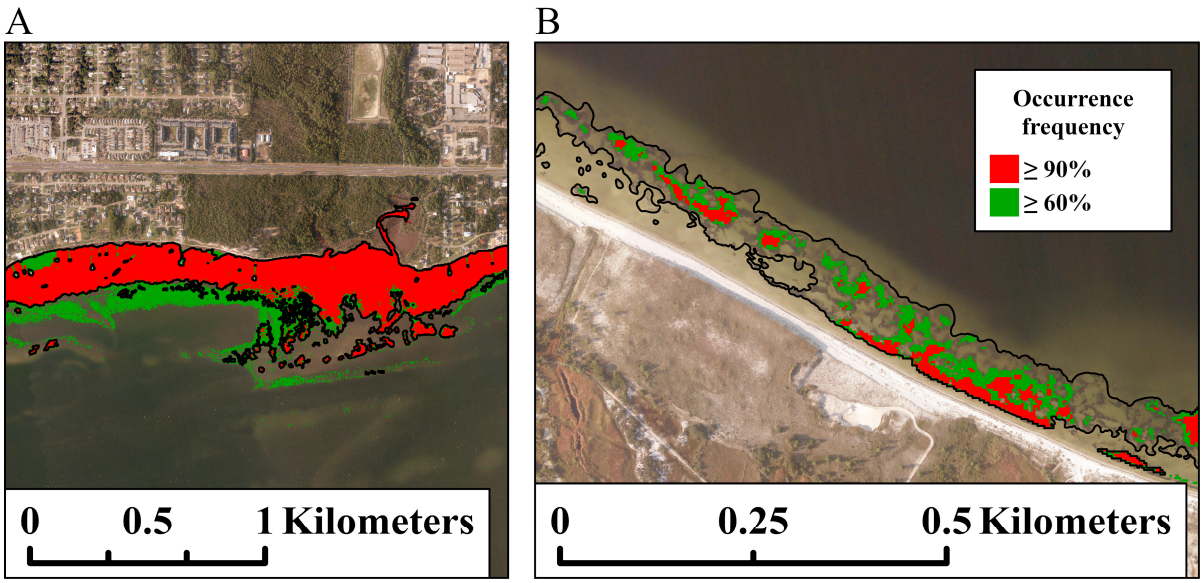

Figure 4. Seagrass area polygons derived from aerial imagery (black lines), and Planet-identified seagrass using *OF* thresholds of ≥60% and ≥90% overlaid on aerial imagery. (**A**) Subset of aerial imagery highlighted as Box 3 in Figure 3; (**B**) subset of aerial imagery highlighted as Box 5 in Figure 3.

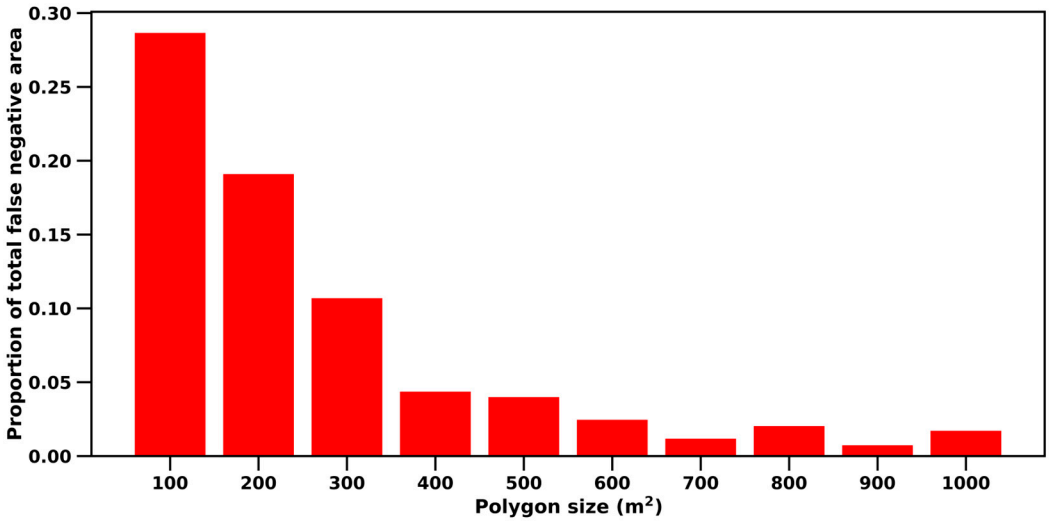

Figure 5. Proportion of false-negative area by polygon size (with *OF* ≥ 60%) for aerial polygons where zero Planet pixels were identified as seagrass.

Previous estimates of seagrass area were determined by hand-delineated polygons drawn on aerial imagery, with areas classified as continuous or patchy (cf. [32,33]). Our

satellite-mapped extent shows that while seagrass has not reached the high coverage observed in 1962, it has expanded by ~1.6 km^2 from the low extents mapped in 1992 and 2003 (Figure 6). Additionally, the seagrass area appears to have remained stable in Santa Rosa Sound since the last mapping project in 2015.

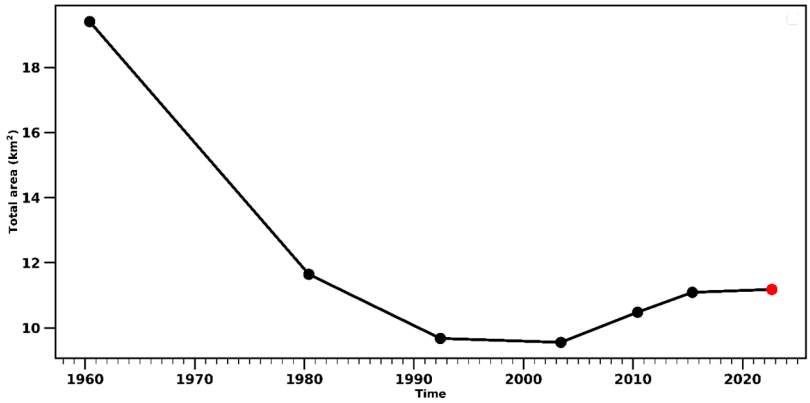

Figure 6. Previous (black) seagrass areal extent for Santa Rosa Sound based on historic data [32,33] and 2022 estimate (red) derived from this analysis. Historical area generated by setting the average patchy density at 50% and summing continuous + patchy × 0.5 areas provided in the literature.

3.2. Leaf Area Index and Above- and Below-Ground Carbon

The mean leaf area index (calculated from all images) was highest near the mouth of Santa Rosa Sound, with maximum values reaching 2.7 m^2 leaf m^{-2} seafloor at East Sabine (Figure 3) and other meadows in that area. LAI decreased to values approaching 1 m^2 leaf m^{-2} seafloor eastward towards the Navarre Bridge. Within the pixels classified as seagrass, the mean LAI throughout the sound was 1.47 ± 0.64 m^2 leaf m^{-2} seafloor, which is consistent with in situ values reported in previous studies (Table 4). The 95% confidence limits of the retrieved LAI also provide us with the lower limit of detection of seagrass at ~0.8 m^2 leaf m^{-2} seafloor. Converting LAI to area-specific above-ground fresh-weight biomass (AGB_{FW}), dry-weight biomass (AGB_{DW}), and below-ground dry-weight biomass (BGB_{DW}) produced mean values for Santa Rosa Sound of 487 g FW m^{-2}, 97 g DW m^{-2}, and 195 g DW m^{-2}, all of which are comparable to independent in situ measurements (Table 4). Summing all the above- and below-ground biomass estimates from each seagrass pixel, Santa Rosa Sound appears to support 3.16 Gg of dry seagrass biomass and 1.11 Gg of carbon (Table 4).

Table 4. Retrieved seagrass density and biomass variables and values reported in the literature, a, b, and c represent the references for the data.

Variable	This Study Mean ± 95% C.L	Other Studies (Dates Collected) Mean ± 1 S.D
LAI (m^2 leaf m^{-2} seafloor) Mean ± 95% CL	1.47± 0.64	[a] 1.16 ± 0.6 (June 2016) [a] 1.78 ± 0.8 (July 2016) [a] 1.85 ± 0.71 (September 2016)
Above-ground fresh biomass (g FW m^{-2})	487 ± 214	[a] 261–625 (June–September 2016) [b] 200–780 (June 2002 and February 2005)
Above-ground dry biomass (g DW m^{-2})	97 ± 42	[b] 50–300 (June 2002 and February 2005) [c] 100–200 (2002, 2004, 2005)
Below-ground dry biomass (g DW m^{-2})	195 ± 84	[c] 200–600 (2002, 2004, 2005)
Total above-ground fresh biomass (Gg)	5.3	
Total above-ground dry biomass (Gg)	1.05	
Total below-ground dry biomass (Gg DW)	2.11	
Total above- + below-ground dry biomass (Gg DW)	3.16	
Total above- + below-ground carbon (Gg C)	1.11	

[a] [38], [b] [30], [c] [44].

3.3. Large Continuous Seagrass Meadows

A large meadow located at Big Sabine Point (total classified area, 7.4 km^2) was clearly identifiable in the Planet imagery (Figures 3 and 7A). Seagrass was identified with an *OF* $\geq$ 90% from the center of the bed to within 2 to 3 pixels (~12 m) of the bed edge (Figure 7B); this high *OF* coincided with the densest part of the bed, where the LAI ranged from 1.4 to 1.8 m^2 m^{-2} (Figure 7C). Near the bed edge, the seagrass *OF* declined to $\geq$60%, with LAIs dropping to 0.8 m^2 leaf m^{-2} seafloor. The extent of the bed determined from the aerial imagery was consistent with the extent identified from Planet at a *OF* $\geq$ 60% threshold (Figure 7B,D), which captured the entirety of the bed, all the way to the deeper edge where seagrass was no longer visible in the aerial imagery.

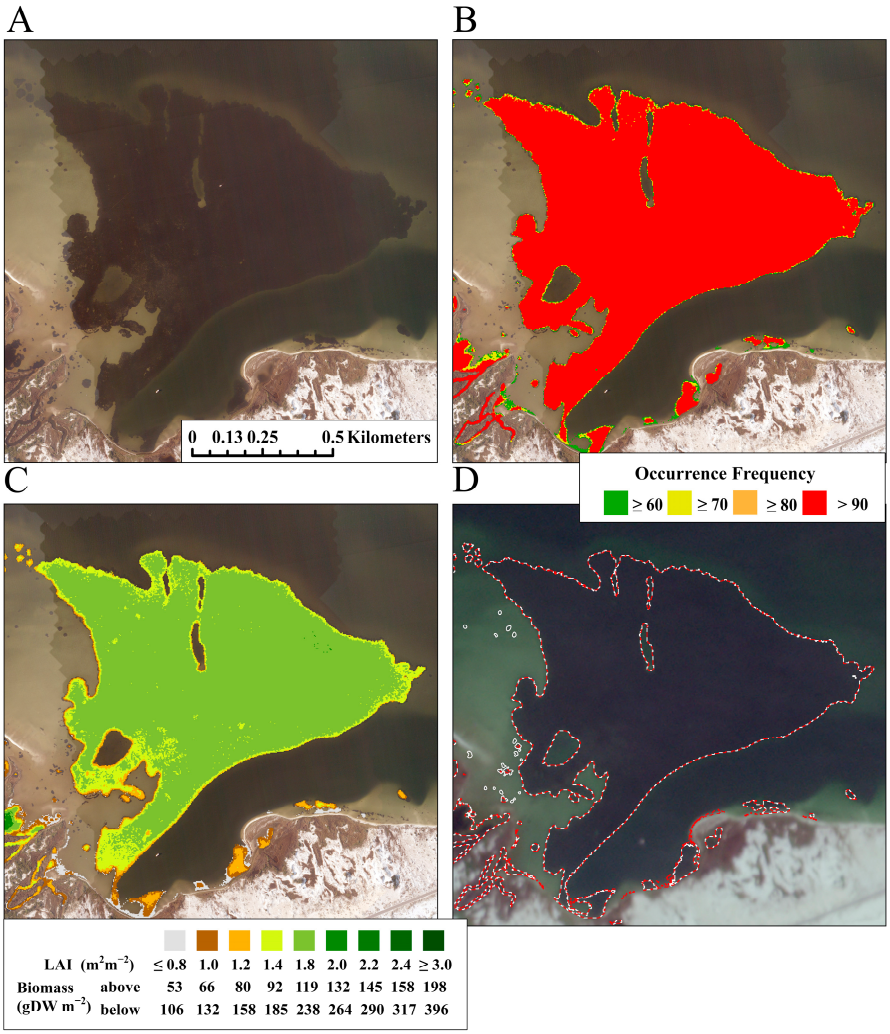

Figure 7. (**A**) RGB representation of a subset of aerial imagery showing the large continuous seagrass meadow at Big Sabine Point in the middle of Santa Rosa Sound (see Figure 3, box 1). (**B**) Seagrass *OF* derived from all satellite images overlaid on the aerial imagery from panel (**A**). (**C**) Mean leaf area index, above-ground biomass, and below-ground biomass overlaid on the aerial imagery from panel (**A**). (**D**) Polygons based on aerial imagery (dashed white lines) and polygons generated for *OF* $\geq$ 60% (dashed red lines) overlaid on Planet imagery.

3.4. Areas of Mixed Density Within Seagrass Meadows

The northern shore of Santa Rosa Sound was characterized by a more or less continuous band of seagrass (Figures 3 and 8A). Residential docks, areas of bare sand, and seagrass patches extending into deeper water were resolved in the Planet imagery (Figure 8B). Continuous seagrass meadows in this area were identified in the Planet imagery with

an *OF* ≥ 90% in the center of the beds, declining to ≥70% at the deeper edges of the beds (Figure 8B). LAIs varied from 1.4 m^2 leaf m^2 seafloor in the center of the beds to <1.0 m^2 leaf m^{-2} seafloor along both the deeper edges of the beds and between some denser patches of seagrass (Figure 8C). The deeper edges of the beds and the edges of the bed next to shallow bare sediment seen in the middle of this image were resolved in the Planet imagery (Figure 8D). In the aerial imagery, there were some dense seagrass patches close to shore with clearly visible bed edges (Figure 8A); the areas between these patches appear to be unvegetated. In the analysis of the Planet imagery, these areas were classified not as bare sediment but as having sparse seagrass coverage (<1.0 m^2 leaf m^2) (Figure 8D).

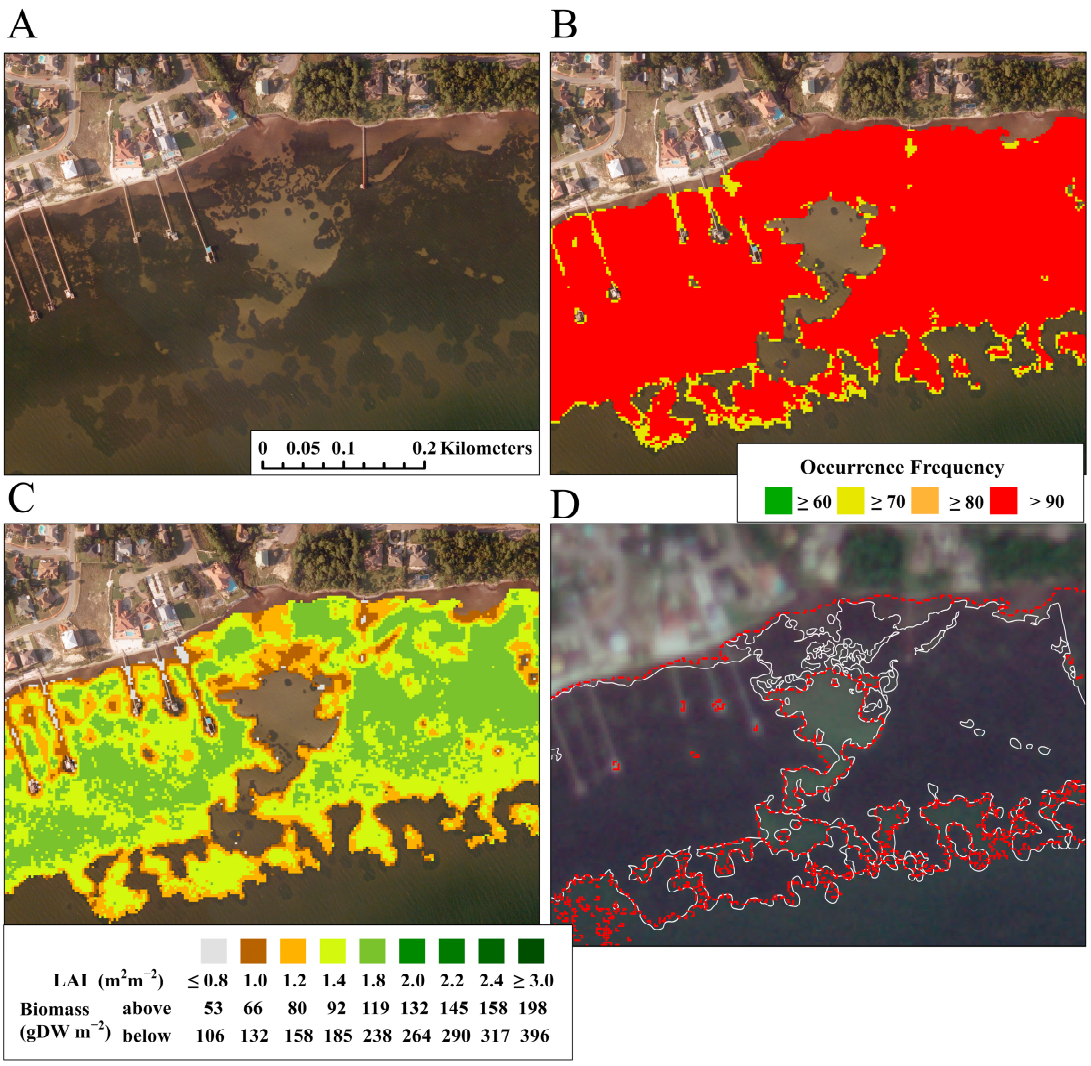

Figure 8. (**A**) RGB representation of a subset of aerial imagery showing a seagrass meadow along the north shore of Santa Rosa Sound. The location of this site is shown in Figure 3, box 2. (**B**) Planet-derived *OF* overlaid on the aerial imagery from panel (**A**). (**C**) Leaf area index, above-ground biomass, and below-ground biomass overlaid on the aerial imagery from panel (**A**). (**D**) Polygons based on aerial imagery (dashed white lines) and polygons generated for *OF* ≥ 60% (dashed red lines) overlaid on Planet imagery.

3.5. Seagrass Meadows Obscured in Aerial Imagery

The aerial coverage of Santa Rosa Sound was limited to one day (22 September 2022), and the photography collected during that pass revealed plumes of suspended sediment along the north shore at the eastern end of the sound near the Navarre Bridge (Figure 9A). The suspended sediment partially obscured the seagrass along the shoreline

and completely concealed the seagrass in the shallow central channel area. In contrast, the Planet constellation provided five useful images with clear skies and no suspended sediment between 8 and 20 September. Mapping with Planet imagery (Figure 9B) reliably identified the seagrass meadows with an *OF* over ≥90% in the central portions of the beds and ≥60% along the deeper edges (Figure 9C). These beds were found to have an LAI of 1.4 to 1.6 m^2 m^{-2} in the center of the beds declining to ~1 m^2 m^{-2} along the deeper edges of the beds (Figure 9C). Due to the obscuration of the beds in the aerial imagery, it is challenging to identify the full extent of the seagrass; however, it does appear that the *OF* ≥ 60% may include false positives along the deep edge of the beds (Figure 9B,D).

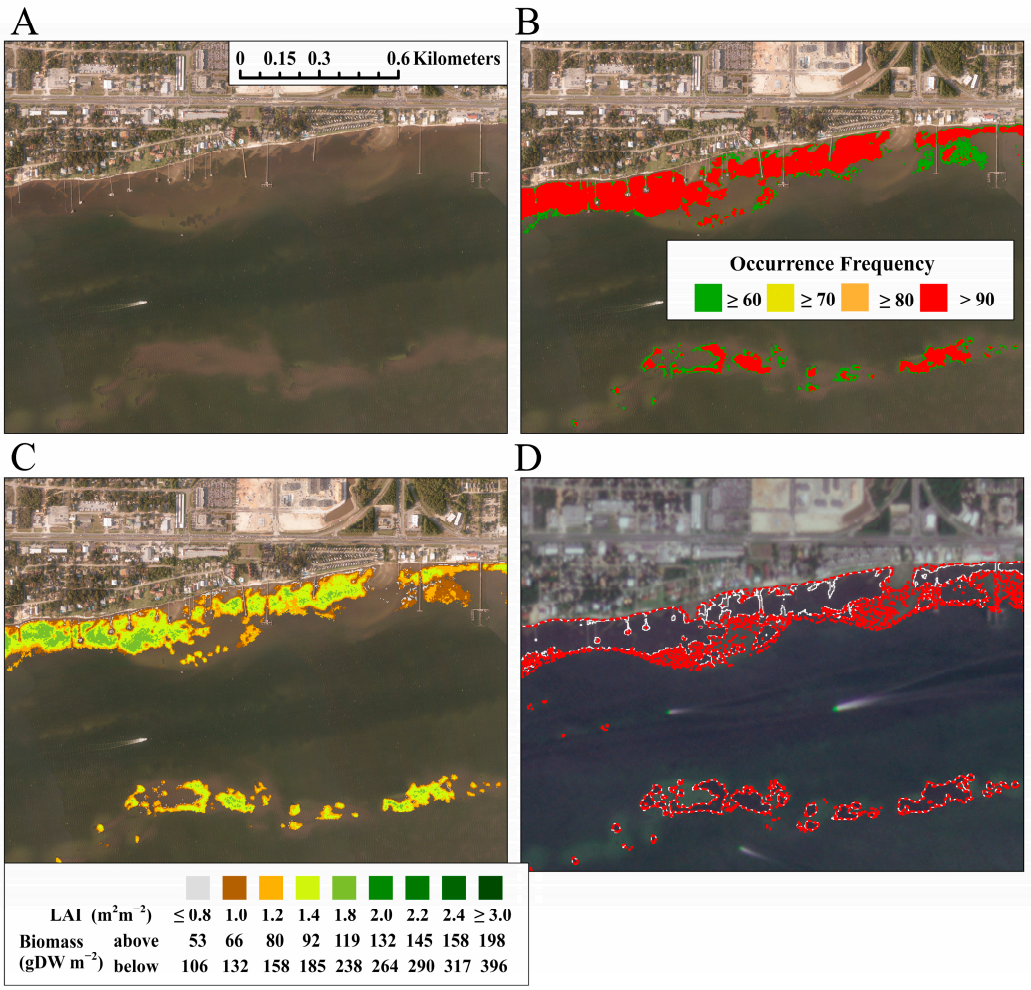

Figure 9. (**A**). Subset of RGB aerial images just west of Navarre Bridge; the location of this site is shown in Figure 3, box 3. Seagrass meadows along the shore and in the middle of Santa Rosa Sound were obscured by suspended sediment plumes in the aerial image (**B**). Planet-derived *OF* overlaid on the aerial imagery from panel (**A**). (**C**) Leaf area index, above-ground biomass, and below-ground biomass overlaid on the aerial imagery from panel (**A**). (**D**) Polygons based on aerial imagery (dashed white lines) and polygons generated from *OF* ≥ 60% (dashed red lines) overlaid on Planet imagery.

3.6. Identification of Small Seagrass Patches

At several locations on the southern (barrier island) shore of Santa Rosa Sound, areas of largely unvegetated sand at depths between 0.4 and 1.0 m were present, transitioning into continuous seagrass meadows in deeper water (Figure 10A). Small patches of seagrass were visible on the sand bank in the aerial photograph that were not resolved in the Planet imagery and covered approximately <18 pixels at Planet resolution (Figure 10A,B). The seagrass meadow on the left side of the image supported an LAI of 1.4 to 1.8 m^2 leaf m^{-2} seafloor and was well resolved in the Planet imagery (Figure 10B,C). The unresolved

patches of seagrass on the sand bank in this example represent 0.03 km^2 of false-negative classifications and provide a patch size limitation of <200 m^2 for the Planet spatial resolution (Figure 10D).

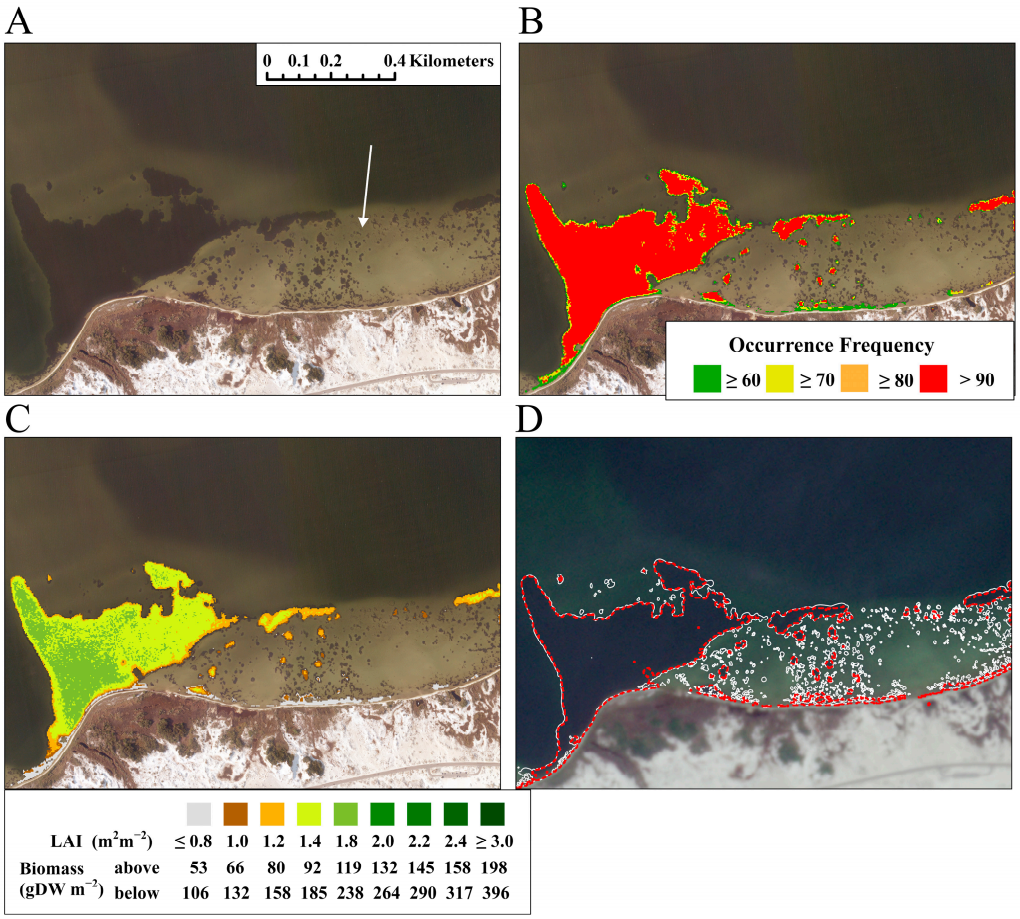

Figure 10. (**A**) Subset of RGB aerial images showing an example of seagrass distribution over a shallow sand bank along the southern shore of Santa Rosa Sound. The location of this site is shown in Figure 3 box 4; the white arrow points to shallow sand with small seagrass patches. (**B**). Planet-derived *OF* overlaid on the aerial imagery from panel (**A**). (**C**) Leaf area index, above-ground biomass, and below-ground biomass overlaid on the aerial imagery from panel (**A**). (**D**) Polygons based on aerial imagery (dashed white lines) and polygons generated for *OF* $\geq$ 60% (dashed red lines) overlaid on Planet imagery.

3.7. Retrieval Uncertainties

Uncertainty in seagrass classification and biomass was assessed by comparing the retrievals from the area common to seven of the Planet images (dashed box in Figure 3). The seagrass area retrieved from each image ranged from 4.24 to 4.60 km^2, with a mean of 4.36 km^2 and 95% confidence interval of 0.1 km^2 (Table 5). Using the $\geq$60% *OF* threshold for the image subsets also generated a seagrass area of 4.37 km^2. The total $AGC_{seagrass}$ ranged from 0.17 to 0.26 Gg across the images, with a mean of 0.22 Gg and a 95% confidence interval of 0.02 Gg (Table 5). It was not possible to generate uncertainty statistics for the seagrass area estimate from the aerial survey because only one image was available.

Table 5. Total area and above-ground carbon retrieved from an overlapping area of seven Planet images.

Image Acquisition Date_Sensor ID	Total Area (km^2)	Total Above-Ground Carbon (Gg)
20220908_247d	4.32	0.25
20220913_2403	4.25	0.26
20220917_2498	4.52	0.19
20220918_249d	4.33	0.21
20220919_2448	4.28	0.21
20220920_2489	4.60	0.24
20220925_2448	4.24	0.17
50% occurrence threshold	4.37	
Mean $\pm$ 95% CI	4.36 $\pm$ 0.10	0.22 $\pm$ 0.02

4. Discussion

The seagrasses within Santa Rosa Sound were largely distributed as expansive, uninterrupted meadows, easily discernible using the ~3 m pixel resolution of Planet imagery. Further, our semi-automated analysis of the Planet imagery effectively classified 95.5% of the seagrass area within the sound, with false positives accounting for 0.62 km^2 at an $OF \geq 60\%$. Increasing the *OF* threshold reduces the true positives (85.7% at $\geq$90%) while also reducing false-positive misclassifications. The classification process leveraged the analysis of all ten clear-sky images captured by Planet sensors throughout September to produce the frequency with which each pixel was classified as seagrass, thus providing confidence in our estimates of seagrass presence, while systematically mitigating small, sporadic misclassifications occurring in only 1 or 2 of the images. A retrieval uncertainty of 0.1 km^2 or 2.3% was calculated from seven individual images that overlapped in area, reflecting the high level of confidence in the robustness of our classification method across different images and the accuracy of the seagrass area estimate.

The detection capability of Planet imagery was most reliable when seagrass patch sizes exceeded 9 to 15 pixels (~200 m^2) and when the LAI was greater than 0.8 m^2 leaf m^{-2} seafloor. The classifier had trouble distinguishing seagrass from sand for small patches and sparse coverage. This limitation arises from a combination of differences in brightness between sand and seagrass, as well as adjacency and edge effects. Consequently, a pixel featuring an equal distribution of bright sand and dark seagrass may be classified as sand due to the brightness of the sand reflectance swamping the dark seagrass reflectance signal. Similarly, with adjacent pixels, the brighter sand reflectance can spill over into neighboring darker seagrass pixels, which may increase the density threshold for their classification as seagrass. Consequently, pixels along the perimeter of a larger bed or surrounding a smaller patch of seagrass (<200 m^2) can be influenced by both effects, meaning that the edge pixels are the most vulnerable to being classified as sand, not seagrass. These factors collectively reduce the accuracy of detecting smaller seagrass patches, as well as the perimeter of larger seagrass meadows.

Previous aerial surveys of Santa Rosa Sound utilized a classification system consisting of two density categories: continuous and patchy. Polygons categorized as patchy were defined as areas smaller than one acre with at least 15% bare sediment visible between seagrass and could have had from 10% to 85% seagrass coverage [45]. In contrast, our objective classification of each pixel allowed us to differentiate bare sediment more completely from seagrass, resulting in a lower but more accurate estimate of the true seagrass abundance because pixels consisting of bare sand were not counted as seagrass. This new satellite-based estimate indicates that the recovery of seagrass in Santa Rosa Sound that started in 2010 has continued and seagrass area is consistent with the last aerial survey in 2015. Future efforts could expand our analysis to the entire Planet archive dating back to 2017, providing insights into shorter-term (<10 years) trends and seasonal variation in seagrass coverage and health that can be linked to environmental factors, such as water

temperature, storms, and changes in water quality on the scale of the entire Sound, as well as specific locations within the system.

The occurrence frequency statistic is instrumental in pinpointing areas of high confidence in seagrass retrieval. In regions where seagrass coverage remains consistent throughout the year, *OF* serves as a reliable indicator of retrieval confidence. This is seen in the uncertainty analysis, where the ≥60% *OF* threshold returned the same seagrass area as the mean area across all seven images used in the uncertainty analysis. The edges of the beds generally have lower *OF* values, which is likely a combination of factors including reduced shoot density, differences in water depth, tidal state (ranging from 0.21 to 0.55 m across the days imaged), and day-to-day fluctuations in water column optical properties, all of which affect the visibility of the seagrass in these marginal edges. It should be noted that in areas where seagrass is seasonal, an annual *OF* becomes more indicative of seasonality rather than retrieval confidence. In such locations, the production of monthly or seasonal *OF* maps, contingent upon image availability, becomes feasible. Subsequently, *OF* can be employed as a gauge of confidence in these seasonal or monthly maps.

The satellite-retrieved mean LAI was comparable with previous in situ measurements of *T. testudinum* LAI at various sites throughout Santa Rosa Sound [38]. As the LAI retrieval is based on absolute reflectance in the green band, incomplete atmospheric correction (residual reflectance) in this band results in the underestimation of LAI, as seen in both Landsat and WorldView-2 images where dark object subtraction was used for atmospheric correction [19,37]. The reliable retrieval of the LAI in Santa Rosa Sound suggests that the Planet atmospherically corrected product supplied for this region was sufficiently effective in LAI estimation. The atmospherically corrected green band in Planet has, in fact, been identified as having the lowest mean absolute relative differences between the atmospherically corrected product and in situ radiances [46] and therefore may be the best band for seagrass biomass retrieval. Future studies should prioritize coincident in situ LAI and biomass measurements with satellite passes to provide confidence analysis for the retrieved LAI.

Scaling our approach for determining seagrass carbon from space to other systems will permit the large-scale, consistent, and cost-effective assessment of seagrass contribution to the coastal Blue Carbon reservoir. Retrieved LAI was used to estimate both above- and below-ground biomass, both of which were found to be within the range of in situ values previously reported for Santa Rosa Sound [30,44]. From the pixel-by-pixel analysis, we estimate a total above-ground standing biomass of 1.05 Gg C in the Santa Rosa Sound seagrass system. Based on blade turnover rates of 2% day^{-1} previously observed in Santa Rosa Sound [38], the annual above-ground carbon represented by seagrass could be as high as 7.4 Gg yr^{-1}, which, when combined with the below-ground carbon of 0.32 Gg, translates to approximately 10,070 tons of CO_2 not circulating in the atmosphere [47]. Although the fate of organic carbon production in Santa Rosa Sound remains uncertain, the material can follow several pathways, including herbivory, incorporation into the local detrital pool within the meadow, or passive transport out of the system via currents and waves [48]

The LAI and biomass estimates that we generated for Santa Rosa Sound sit between the extremes of other sites along the Florida Gulf Coast, being less than that reported for St. Joseph Bay [37], but higher than those reported for Saint Andrews Bay and Saint George Sound. These variations in seagrass density and biomass likely reflect differences in water quality and anthropogenic impacts across these sites. Understanding these spatial patterns is crucial in identifying the drivers of seagrass health and resilience along the Gulf Coast, which is essential for conservation and restoration efforts. Using satellite data to retrieve biomass and estimate potential carbon sequestration represents a significant advancement toward scalable blue carbon assessments. By improving our ability to quantify the carbon stored in these ecosystems, we can better understand their role in mitigating climate change, supporting Blue Carbon initiatives, and informing conservation strategies.

5. Conclusions

Our analysis of Planet imagery from Santa Rosa Sound, FL, indicates that the distribution and abundance of seagrass populations appears to be stable relative to previous aerial and ground-based surveys going back to 1980. Despite providing lower spatial resolution, the Planet data generated highly reliable estimates of seagrass distribution that compared favorably with estimates from high-resolution aerial imagery. Further, the ability to quantify seagrass abundance from radiometrically calibrated and atmospherically corrected values of R_{rs} in this optically complex coastal lagoon represents a considerable improvement over the relative abundances typically generated from aerial imagery. The capacity for increased observational frequency provided by the Planet constellation (in this case, 10 useful images in 1 month) required no logistics costs for image tasks, which shows potential for the generation of comprehensive time-series data that can provide a deeper understanding of seagrass dynamics over time. The ability to quantify absolute biomass also provides an avenue for estimating carbon sequestration and for improving our understanding of the ecological roles that seagrass meadows play in coastal environments. A key strength of our approach is the portability and accessibility of our methodology, which can be applied to other coastal regions with minimal computational requirements. Requiring only laptop-scale computational power and internet access to the Planet archive, this methodology opens up new possibilities for seagrass monitoring in resource-constrained settings, enabling the more widespread adoption of advanced remote sensing techniques.

Author Contributions: Conceptualization: V.J.H., R.C.Z., K.L.H.J. and D.A.B. Formal Analysis: V.J.H. and R.C.Z. Resources: K.L.H.J., D.A.B., V.J.H. and R.C.Z. Data Curation: V.J.H. and D.A.B. Writing—Original Draft: V.J.H. Writing—Review and Editing: R.C.Z., K.L.H.J. and D.A.B. Visualization: V.J.H. All authors have read and agreed to the published version of the manuscript.

Funding: Funding Acquisition: Ken Heck and Dorothy Byron. Funding for aerial image acquisition was provided by the Pensacola and Perdido Bays Estuary Program through U.S. Environmental Protection Cooperative Agreement No. 00D81118.

Data Availability Statement: Data for image processing were derived from SuperDove satellites from the PlanetScope constellation, accessed via NASA's Commercial SmallSat Data Acquisition (CSDA) Program.

Conflicts of Interest: The authors declare no conflict of interest.

References

1. Lima, M.A.C.; Bergamo, T.F.; Ward, R.D.; Joyce, C.B. A review of seagrass ecosystem services: Providing nature-based solutions for a changing world. *Hydrobiologia* **2023**, *850*, 2655–2670. [CrossRef]
2. McDevitt-Irwin, J.M.; Iacarella, J.C.; Baum, J.K. Reassessing the nursery role of seagrass habitats from temperate to tropical regions: A meta-analysis. *Mar. Ecol. Prog. Ser.* **2016**, *557*, 133–143. [CrossRef]
3. Heck, K.L.; Thoman, T.A. The nursery role of seagrass meadows in the upper and lower reaches of the Chesapeake Bay. *Estuaries* **1984**, *7*, 70–92. [CrossRef]
4. Fonseca, M.S.; Fisher, J.S.; Zieman, J.C.; Thayer, G.W. Influence of the seagrass, *Zostera marina* L. on current flow. *Estuar. Coast. Shelf Sci.* **1982**, *15*, 351–364. [CrossRef]
5. Fonseca, M.S.; Fisher, J.S. A comparison of canopy friction and sediment movement between four species of seagrass with reference to their ecology and restoration. *Mar. Ecol. Prog. Ser.* **1986**, *29*, 5–22. [CrossRef]
6. Koch, E.W.; Gust, G. Water flow in tide-and wave-dominated beds of the seagrass Thalassia testudinum. *Mar. Ecol. Prog. Ser.* **1999**, *184*, 63–72. [CrossRef]
7. Koch, E.W. Beyond light: Physical, geological, and geochemical parameters as possible submersed aquatic vegetation habitat requirements. *Estuaries* **2001**, *24*, 1–17. [CrossRef]
8. De Boer, W. Seagrass–sediment interactions, positive feedbacks and critical thresholds for occurrence: A review. *Hydrobiologia* **2007**, *591*, 5–24. [CrossRef]
9. Potouroglou, M.; Bull, J.C.; Krauss, K.W.; Kennedy, H.A.; Fusi, M.; Daffonchio, D.; Mangora, M.M.; Githaiga, M.N.; Diele, K.; Huxham, M. Measuring the role of seagrasses in regulating sediment surface elevation. *Sci. Rep.* **2017**, *7*, 11917. [CrossRef]
10. Ondiviela, B.; Losada, I.J.; Lara, J.L.; Maza, M.; Galván, C.; Bouma, T.J.; van Belzen, J. The role of seagrasses in coastal protection in a changing climate. *Coast. Eng.* **2014**, *87*, 158–168. [CrossRef]

11. Mtwana Nordlund, L.; Koch, E.W.; Barbier, E.B.; Creed, J.C. Seagrass ecosystem services and their variability across genera and geographical regions. *PLoS ONE* **2016**, *11*, e0163091. [CrossRef]
12. Chmura, G.; Short, F.; Torio, D.; Arroyo-Mora, P.; Fajardo, P.; Hatvany, M.; van Ardenne, L. *North America's Blue Carbon: Assessing seagrazss, Salt Marsh and Mangrove Distribution and Carbon Sinks: Project Report*; Commission for Environmental Cooperation: Montreal, QC, Canada, 2016.
13. Orth, R.J.; Dennison, W.C.; Gurbisz, C.; Hannam, M.; Keisman, J.; Landry, J.B.; Lefcheck, J.S.; Moore, K.A.; Murphy, R.R.; Patrick, C.J. Long-term annual aerial surveys of submersed aquatic vegetation (SAV) support science, management, and restoration. *Estuaries Coasts* **2022**, *45*, 1012–1027. [CrossRef]
14. McKenzie, L.J.; Nordlund, L.M.; Jones, B.L.; Cullen-Unsworth, L.C.; Roelfsema, C.; Unsworth, R.K. The global distribution of seagrass meadows. *Environ. Res. Lett.* **2020**, *15*, 074041. [CrossRef]
15. Orth, R.J.; Williams, M.R.; Marion, S.R.; Wilcox, D.J.; Carruthers, T.J.; Moore, K.A.; Kemp, W.M.; Dennison, W.C.; Rybicki, N.; Bergstrom, P. Long-term trends in submersed aquatic vegetation (SAV) in Chesapeake Bay, USA, related to water quality. *Estuaries Coasts* **2010**, *33*, 1144–1163. [CrossRef]
16. Sherwood, E.T.; Greening, H.S.; Johansson, J.R.; Kaufman, K.; Raulerson, G.E. Tampa Bay (Florida, USA) documenting seagrass recovery since the 1980's and reviewing the benefits. *Southeast. Geogr.* **2017**, *57*, 294–319. [CrossRef]
17. Metz, J.L.; Harris, R.J.; Arrington, D.A. Seasonal occurrence patterns of seagrass should influence resource assessment and management decisions: A case study in the Indian River Lagoon and Loxahatchee River Estuary, Florida. *Reg. Stud. Mar. Sci.* **2020**, *34*, 101093. [CrossRef]
18. Kaufman, K.A.; Bell, S.S. The Use of Imagery and GIS Techniques to Evaluate and Compare Seagrass Dynamics across Multiple Spatial and Temporal Scales. *Estuaries Coasts* **2020**, *45*, 1028–1044. [CrossRef]
19. Lebrasse, M.C.; Schaeffer, B.A.; Coffer, M.; Whitman, P.J.; Zimmerman, R.C.; Hill, V.J.; Islam, K.A.; Li, J.; Osburn, C.L. Temporal Stability of Seagrass Extent, Leaf Area, and Carbon Storage in St. Joseph Bay, Florida: A Semi-automated Remote Sensing Analysis. *Estuaries Coasts* **2022**, *45*, 2082–2101. [CrossRef]
20. Misbari, S.; Hashim, M. Change Detection of Submerged Seagrass Biomass in Shallow Coastal Water. *Remote Sens.* **2016**, *8*, 200. [CrossRef]
21. Pu, R.; Bell, S. Mapping seagrass coverage and spatial patterns with high spatial resolution IKONOS imagery. *Int. J. Appl. Earth Obs.* **2017**, *54*, 145–158. [CrossRef]
22. Phinn, S.; Roelfsema, C.; Dekker, A.; Brando, V.; Anstee, J. Mapping seagrass species, cover and biomass in shallow waters: An assessment of satellite multi-spectral and airborne hyper-spectral imaging systems in Moreton Bay (Australia). *Remote Sens. Environ.* **2008**, *112*, 3413–3425. [CrossRef]
23. Roelfsema, C.M.; Lyons, M.; Kovacs, E.M.; Maxwell, P.; Saunders, M.I.; Samper-Villarreal, J.; Phinn, S.R. Multi-temporal mapping of seagrass cover, species and biomass: A semi-automated object based image analysis approach. *Remote Sens. Environ.* **2014**, *150*, 172–187. [CrossRef]
24. Wicaksono, P.; Maishella, A.; Arjasakusuma, S.; Lazuardi, W.; Harahap, S.D. Assessment of WorldView-2 images for aboveground seagrass carbon stock mapping in patchy and continuous seagrass meadows. *Int. J. Remote Sens.* **2022**, *43*, 2915–2941. [CrossRef]
25. Coffer, M.; Schaeffer, B.A.; Zimmerman, R.C.; Hill, V.; Li, J.; Islam, K.A.; Whitman, P.J. Performance across WorldView-2 and RapidEye for reproducible seagrass mapping. *Remote Sens. Environ.* **2020**, *250*, 112036. [CrossRef] [PubMed]
26. Koedsin, W.; Intararuang, W.; Ritchie, R.J.; Huete, A. An Integrated Field and Remote Sensing Method for Mapping Seagrass Species, Cover, and Biomass in Southern Thailand. *Remote Sens.* **2016**, *8*, 292. [CrossRef]
27. Zoffoli, M.L.; Gernez, P.; Rosa, P.; Le Bris, A.; Brando, V.E.; Barillé, A.-L.; Harin, N.; Peters, S.; Poser, K.; Spaias, L. Sentinel-2 remote sensing of Zostera noltei-dominated intertidal seagrass meadows. *Remote Sens. Environ.* **2020**, *251*, 112020. [CrossRef]
28. Wicaksono, P.; Lazuardi, W. Assessment of PlanetScope images for benthic habitat and seagrass species mapping in a complex optically shallow water environment. *Int. J. Remote Sens.* **2018**, *39*, 5739–5765. [CrossRef]
29. Veettil, B.K.; Ward, R.D.; Lima, M.D.A.C.; Stankovic, M.; Hoai, P.N.; Quang, N.X. Opportunities for seagrass research derived from remote sensing: A review of current methods. *Ecol. Indic.* **2020**, *117*, 106560. [CrossRef]
30. Caffrey, J.M.; Albrecht, B.B.; Capps, R. *Seagrass abundance and productivity in Pensacola Bay and Santa Rosa Sound: Final Technical Report*; University of West Florida: Ferry Pass, FL, USA, 2017.
31. Presley, R.; Caffrey, J.M. Nitrogen fixation in subtropical seagrass sediments: Seasonal patterns in activity in Santa Rosa Sound, Florida, USA. *J. Mar. Sci. Eng.* **2021**, *9*, 766. [CrossRef]
32. Lewis, M.A.; Devereux, R.; Bourgeois, P. Seagrass distribution in the Pensacola Bay system, northwest Florida. *Gulf Caribb. Res.* **2008**, *20*, 21–28. [CrossRef]
33. Bryon, D.; Heck, K.L., Jr.; Kebart, K.; Caffrey, J.M.; Harvey, A.; Fugate, B.; Carlson, P.R., Jr.; Johnsey, E. Summary Report for the Pensacola Region. In *Seagrass Integrated Mapping and Monitoring Report No. 3*; Carlson, P.R., Jr., Johnsey, E., Eds.; Fish and Wildlife Research Institute Technical Report TR-17 version 3; Florida Fish and Wildlife Conservation Commission: St. Petersburg, FL, USA, 2018.
34. American Society for Photogrammetry and Remote Sensing. New ASPRS positional accuracy standards for digital geospatial data. *Photogramm. Eng. Remote Sens.* **2015**, *81*, 277. [CrossRef]

35. Cooperative Institute for Research in Environmental Sciences (CIRES) at the University of Colorado Boulder. Continuously Updated Digital Elevation Model (CUDEM)—1/9 Arc-Second Resolution Bathymetric-Topographic Tiles. 2014. Available online: https://coast.noaa.gov/dataviewer/#/lidar/search/where:ID=8483 (accessed on 12 January 2023).
36. Hill, V.J.; Zimmerman, R.C.; Bissett, P.; Dierssen, H.M.; Kohler, D. Evaluating Light Availability, Seagrass Biomass, and Productivity Using Hyperspectral Airborne Remote Sensing in Saint Joseph's Bay, Florida. *Estuaries Coasts* **2014**, *37*, 1467–1489. [CrossRef]
37. Hill, V.J.; Zimmerman, R.C.; Bissett, P.; Kohler, D.; Schaeffer, B.; Coffer, M.; Li, J.; Islam, K.A. Impact of Atmospheric Correction on Classification and Quantification of Seagrass Density from WorldView-2 Imagery. *Remote Sens.* **2023**, *15*, 4715. [CrossRef]
38. Yarbro, L.A.; Carlson, P.R.; Heck, K.L.; Byron, D.; Brooke, S.; Fitzhugh, L.; Scolaro, S.; Albrecht, B.; Presley, R.; Caffrey, J.M. Biomass and Productivity of Thalassia testudinum in Estuaries of the Florida Panhandle. *Gulf Caribb. Res.* **2023**, *34*, 69–78. [CrossRef]
39. Voss, K.J.; Mobley, C.D.; Sundman, L.K.; Ivey, J.E.; Mazel, C.H. The spectral upwelling radiance distribution in optically shallow waters. *Limnol. Oceanogr.* **2003**, *48*, 364–373. [CrossRef]
40. Mobley, C.D. *Light and Water: Radiative Transfer in Natural Waters*; Academic Press: San Diego, CA, USA, 1994.
41. van Tussenbroek, B.I. Above- and below-ground biomass and production by Thalassia tesudinum in a tropical reef. *Aquat. Bot.* **1998**, *61*, 69–82. [CrossRef]
42. Sfriso, A.; Ghetti, P.F. Seasonal variation in biomass, morphometric parameters and production of seagrasses in the lagoon of Venice. *Aquat. Bot.* **1998**, *61*, 207–223. [CrossRef]
43. Hemminga, M.A.; Duarte, C.M. *Seagrass Ecology Seagrass*; Cambridge University Press: Cambridge, UK, 2000.
44. Devereux, R.; Yates, D.F.; Aukamp, J.; Quarles, R.L.; Jordan, S.J.; Stanley, R.S.; Eldridge, P.M. Interactions of Thalassia testudinum and sediment biogeochemistry in Santa Rosa Sound, NW Florida. *Mar. Biol. Res.* **2011**, *7*, 317–331. [CrossRef]
45. Schwenning, L.; Bruce, T.; Handley, L.R. Pensacola Bay. In *Seagrass Status and Trends in the Northern Gulf of Mexico: 1940–2022*; Handley, L., Altsman, D., DeMay, R., Eds.; USGS Publications Warehouse: Reston, VA, USA, 2007; Volume 2006–5287, pp. 129–142.
46. Vanhellemont, Q. Evaluation of eight band SuperDove imagery for aquatic applications. *Opt. Express* **2023**, *31*, 13851–13874. [CrossRef]
47. Howard, J.; Hoyt, S.; Isensee, K.; Telszewski, M.; Pidgeon, E. (Eds.) *Coastal Blue Carbon: Methods for Assessing Carbon Stocks and Emissions Factors in Mangroves, Tidal Salt Marshes, and Seagrasses*; Conservation International, Intergovernmental Oceanographic Commission of UNESCO; International Union for Conservation of Nature: Arlington, Virginia, USA, 2014. Available online: https://www.unep.org/resources/publication/coastal-blue-carbon-methods-assessing-carbon-stocks-and-emissions-factors (accessed on 12 November 2024).
48. Heck, K.L.; Carruthers, T.J.; Duarte, C.M.; Hughes, A.R.; Kendrick, G.; Orth, R.J.; Williams, S.W. Trophic transfers from seagrass meadows subsidize diverse marine and terrestrial consumers. *Ecosystems* **2008**, *11*, 1198–1210. [CrossRef]